

A CMOS Passive LPTV Nonmagnetic Circulator and Its Application in a Full-Duplex Receiver

Negar Reiskarimian, *Student Member, IEEE*, Jin Zhou, *Member, IEEE*, and Harish Krishnaswamy, *Member, IEEE*

Abstract—Recently, we demonstrated the first CMOS nonmagnetic nonreciprocal passive circulator based on N-path filters that uses time variance to break reciprocity. Here, the analysis of performance metrics, such as loss, isolation, linearity, and tuning range, is presented in terms of the design parameters. The analysis is verified by the measured performance of a 65-nm CMOS circulator prototype that exhibits 1.7 dB of loss in the transmitter-antenna (TX-ANT) and antenna-receiver (ANT-RX) paths, and has high isolation [TX-RX, up to 50 dB through tuning and 20-dB bandwidth (BW) of 32 MHz] and a tuning range of 610–850 MHz. Through an architectural feature specifically designed to enhance TX linearity, the circulator achieves an in-band TX-ANT input-referred third-order intercept point (IIP3) of +27.5 dBm, nearly two orders of magnitude higher than the ANT-RX IIP3 of +8.7 dBm. The circulator is also integrated with a self-interference-canceling full-duplex (FD) RX featuring an analog baseband (BB) SI canceller. The FD RX achieves 42-dB on-chip SI suppression across the circulator and analog BB domains over a 12-MHz signal BW. In conjunction with digital SI and its input-referred third-order intermodulation (IM3) cancellation, the FD RX demonstrates 85-dB overall SI suppression, enabling an FD link budget of −7-dBm TX average output power and −92-dBm noise floor.

Index Terms—Circulator, CMOS, full-duplex (FD) wireless, interference cancellation, nonreciprocity.

I. INTRODUCTION

FULL-DUPLEX (FD) wireless is an emerging wireless communication paradigm, which has attracted a lot of attention in recent years [1], [2]. FD operation involves simultaneous transmission and reception at the same frequency, potentially resulting in significant improvement in wireless network performance, such as spectral efficiency, link capacity, and network latency [2]–[4].

While FD wireless is promising, there are several fundamental challenges associated with FD operation. The first challenge is the tremendous amount of the transmitter (TX) self-interference (SI) at the same frequency as the desired signal. Short-range wireless applications relax FD system requirements [5]–[7], but an FD system with −6-dBm transmit power, 10-MHz signal bandwidth (BW), and 12-dB NF budget

Manuscript received August 6, 2016; revised November 27, 2016 and December 30, 2016; accepted December 31, 2016. Date of publication March 1, 2017; date of current version April 20, 2017. This work was supported by the DARPA ACT and RF-FPGA programs. This paper was approved by Associate Editor Pietro Andreani.

N. Reiskarimian and H. Krishnaswamy are with the Department of Electrical Engineering, Columbia University, New York, NY 10027 USA (e-mail: harish@ee.columbia.edu).

J. Zhou is with the Department of Electrical and Computer Engineering, University of Illinois at Urbana-Champaign, Champaign, IL 61801 USA.

Color versions of one or more of the figures in this paper are available online at <http://ieeexplore.ieee.org>.

Digital Object Identifier 10.1109/JSSC.2017.2647924

still requires 86 dB of SI suppression to reach the −92-dBm noise floor. To achieve such a high degree of SI suppression, cancellation must be performed across the antenna [8], [9], analog/RF [5], [7], [8], [10]–[13], and digital domains [1], [7]. Another fundamental challenge is related to the FD antenna interface. As shown in Table I, reported FD antenna interfaces can be divided into three categories, namely, antenna pairs [8], [9], [14], electrical-balance duplexers [15]–[18], and nonreciprocal circulators [6], [7], [19]–[23]. Among them, shared-antenna interfaces, such as the electrical-balance duplexers and circulators, are more favorable as they enable compact form factor, translate easily to MIMO and antenna diversity applications, and ease system design through wireless channel reciprocity. However, reciprocal FD shared-antenna interfaces, such as electrical-balance duplexers [15]–[18], feature a fundamental minimum of 3-dB loss (typically higher when parasitic losses are factored in). Passive nonreciprocal circulators typically require the use of magnetic materials (ferrites [19]), making them bulky, expensive, and not amenable to CMOS integration. Circulators that exploit the inherent nonreciprocity of active devices [6], [20]–[22] are limited by the noise and nonlinearity introduced by the active devices [24]. In other words, the realization of compact CMOS-compatible FD shared-antenna interfaces with low loss, low noise, high linearity, and high TX-to-receiver (RX) isolation is an important open challenge.

In [23], we introduced a new circulator concept based on the phase-nonreciprocal behavior of two-port linear periodically time-varying (LPTV) N-path filters when phase-shifted clock signals are applied to the input and output sets of switches, resulting in the first CMOS nonmagnetic passive circulator. In [7], we reported an FD RX, which integrated the circulator with additional analog baseband (BB) SI cancellation. This FD RX: 1) enables a compact FD radio with an integrated low-loss shared-antenna interface; 2) achieves 42-dB on-chip SI suppression across the circulator and analog BB domains over 12-MHz signal BW; and 3) demonstrates 85-dB overall SI suppression in conjunction with digital SI cancellation (SIC) and SI input-referred third-order intermodulation (IM3) distortion cancellation, enabling an FD link budget of −7-dBm TX average output power and −92-dBm noise floor.

This paper provides additional background information, a system-level analysis of the short-range FD radio in Section II, detailed analytical treatments and design guidelines for insertion loss, isolation, linearity, and tuning range of the circulator in Section III, implementation details of the 65-nm CMOS 0.6–0.8-GHz circulator and FD RX in

TABLE I
COMPARISON OF ANTENNA INTERFACES FOR FD RADIOS

| | Antenna Pair [8],[9],[14] | Shared-Antenna Interface | | | |
|---------------------|---------------------------|--|--|--|---|
| | | Reciprocal electrical-balance duplexer [15]–[18] | Non-reciprocal ferrite circulator [19] | Non-reciprocal active circulator [6],[20]–[22] | Non-reciprocal N-path-filter-based passive circulator (this work) |
| Form Factor | ✗ | ✓ | ✗ | ✓ | ✓ |
| Insertion Loss | ✓ | ✗ | ✓ | ✓ | ✓ |
| Noise/ Linearity | ✓ | ✗ / ✓ | ✓ | ✗ | ✓ |
| Channel Reciprocity | ✗ | ✓ | ✓ | ✓ | ✓ |
| CMOS Integration | ✓ | ✓ | ✗ | ✓ | ✓ |

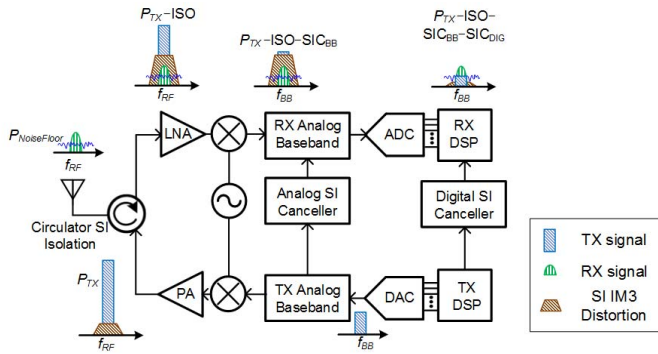


Fig. 1. FD transceiver block diagram with SI suppression across the circulator, analog, and digital domains.

Section IV, and a description of the measurement results and digital SIC algorithm in Section V. Section VI concludes this paper.

II. SYSTEM REQUIREMENTS

The block diagram of the short-range FD wireless transceiver is shown in Fig. 1. The TX signal at power amplifier output includes the TX main signal (P_{TX}) and its nonlinear distortion. The integrated circulator exhibits a certain amount of TX-to-RX isolation (ISO). SIC in the analog domain taps from the TX analog BB and cancels the SI at the RX analog BB. Finally, SIC in the digital domain suppresses both the main SI and the associated distortion signal generated by the TX, circulator, RX, and analog SI canceller.

We assume a short-range wireless system with 10-MHz RX BW and 12-dB RX NF (N_{FRX}), which results in an RX input-referred noise floor ($P_{NoiseFloor}$) of -92 dBm¹. Given a -6 -dBm P_{TX} , the required overall SIC can be calculated as -6 dBm $- (-92$ dBm) $= 86$ dB and is distributed across the circulator, analog, and digital domains, as shown in Fig. 1. Assuming a required SNR of 15 dB, 2-dBi TX and RX dipole antenna gain, implementation losses of 5 dB, 15-dB margin for signal fading, and 5-dB (3 \times) sensitivity degradation due to the residual SI and its IM3, the link budget of -6 dBm $+ 4$ dBi $- (-92$ dBm $+ 5$ dB) $- 15$ dB $- 5$ dB $- 15$ dB $= 50$ dB translates to a transmission distance of 10 m at a frequency of 750 MHz.

¹ $P_{NoiseFloor}$ is the original half-duplex noise floor.

SI suppression in the circulator and analog domains is critical to relaxing the analog-to-digital converter (ADC) dynamic range (DR) requirement. At the ADC input, assuming an identical power level for the main SI and its associated distortion signal, the required ADC DR can be calculated as $DR_{ADC} = (P_{TX-ISO-SIC_{BB}} + 6) - (P_{NoiseFloor} - 6)$, where SIC_{BB} is the amount of SIC achieved in the analog domain. We have included a 6-dB margin at both ends².

The SI suppression in the circulator and analog domains also determines the required RX effective in-band (IB) input-referred third-order intercept point (IIP3) (i.e., IIP3 under analog SIC). Let us assume that the integrated circulator and the SI-canceling RX contribute equally to the SI-induced distortion signal at the ADC input. Since we have assumed that the SI-induced distortion signal at the ADC input has the same power level as the residual main SI after the circulator isolation and analog SIC, the RX effective IB IIP3 can be calculated as

$$IIP_{3,RX,eff} = (P_{TX-ISO} - 3) + \frac{1}{2}(SIC_{BB} + 3) \quad (1)$$

where the single tone power of a two-tone main SI at the RX input is $P_{TX-ISO} - 3$ and the IM3 signals generated by the RX are below the main SI by $SIC_{BB} + 3$. The 3-dB margin is for the IM3 signals generated by the integrated circulator. Similarly, the TX-port-referred IP3 of the integrated circulator's TX-to-RX isolation can be calculated as

$$IIP_{3,Circ,ISO} = P_{TX} - 3 + \frac{1}{2}(SIC_{BB} + 3). \quad (2)$$

Equations (1) and (2) indicate that enhancing SIC_{BB} beyond a certain point carries no benefit. Beyond this point, more SIC in the analog BB does not relax the ADC DR requirement, since SI IM3 products will dominate the residual SI at the ADC input. It should be noted that a higher circulator isolation relaxes both the ADC DR and the SI-canceling RX effective IIP3 requirements. Finally, the required SIC in the digital domain for the main SI and the SI-induced IM3 signals can be calculated as $P_{TX} - P_{NoiseFloor} - ISO - SIC_{BB}$ each.

Assuming 20-dB isolation from the circulator and $SIC_{BB} = 20$ dB, we can calculate ADC DR as 58 dB (2 \times 6-dB margin is included as mentioned before), RX effective IIP3

² 3 dB of the 12-dB margin accounts for the addition of the residual SI and its distortion signal.

TABLE II
SUMMARY OF THE FD SYSTEM SPECIFICATIONS

| | | Specifications |
|---|---|----------------------|
| System Definition | TX average output power | -6 dBm |
| | TX signal bandwidth | 10 MHz |
| | RX NF | 12 dB |
| | RX noise floor | -92 dBm [#] |
| | Total SIC | 86 dB |
| | Link range@750MHz* | 10 m |
| Analog/RF SIC Budget | Circulator isolation | 20 dB |
| | Analog BB SIC | 20 dB |
| Analog/RF Front-End Circuit Performance | DR _{ADC} | 58 dB ^{\$} |
| | RX Effective IIP ₃ | -17.5 dBm |
| | Circulator TX-port-referred ISO IP ₃ | +2.5 dBm |
| Digital SIC Budget | Digital SIC – Linear | 46 dB |
| | Digital SIC – IM3 | 46 dB |

* Assume a required SNR value of 15 dB, 2 dBi TX and RX dipole antenna gain, implementation losses of 5 dB, 15 dB margin for signal fading, and 5 dB sensitivity degradation due to the residual SI and its IM3.

[#]Half-duplex noise figure.

^{\$}12 dB margin has been added to DR_{ADC}.

as -17.5 dBm, and circulator ISO IIP₃ (IIP_{3,Circ,ISO}) as +2.5 dBm. In addition, 46-dB SIC is required in the digital domain for both the main SI and the SI-induced IM3 signal. Table II summarizes the FD system specifications. As will be seen in Section IV, the TX power handling of our FD implementation is dictated by the digital SIC and the RX effective IIP₃, which meet these aforementioned requirements. The integrated circulator's linearity exceeds the requirements dictated by the -6-dBm TX power level.

III. INTEGRATED NONMAGNETIC PASSIVE LPTV CIRCULATOR

Passive linear time-invariant (LTI) systems based on conventional materials are reciprocal. A matched three-port reciprocal antenna interface, such as the electrical-balance duplexer, theoretically necessitates a minimum of 3-dB loss (higher, in practice, due to parasitics) in the TX-ANT and ANT-RX paths. However, nonreciprocal circulators, which break time-reversal symmetry, can avoid this fundamental 3-dB loss. Nonreciprocity has conventionally been achieved using magnetic materials that exhibit the Faraday effect, such as ferrites, or active devices. Ferrite-based circulators are bulky, expensive, and incompatible with CMOS fabrication, and require an external magnetic bias. Circulators based on active devices suffer from poor linearity and noise performance [24].

Reciprocity can also be broken by violating time invariance. Passive linear time-varying systems have been shown to enable nonreciprocal behavior [25]–[27]. In [23], we introduced a new circulator concept based on the phase-nonreciprocal behavior of phase-shifted two-port LPTV N-path filters. Recently, N-path filters have drawn significant research interest due

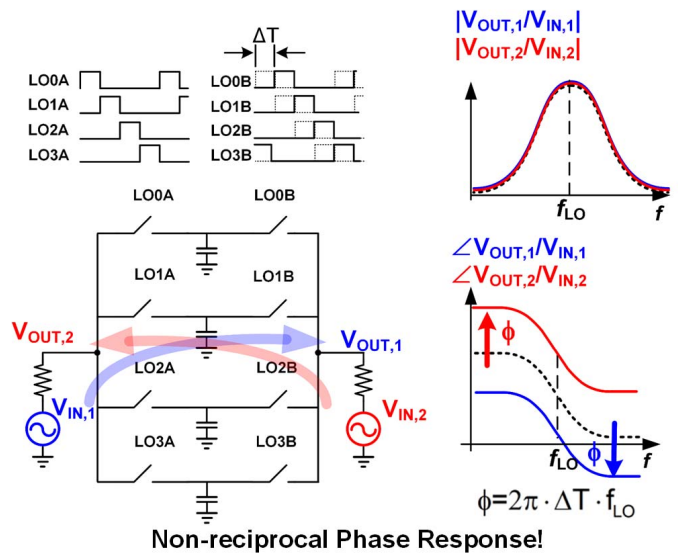


Fig. 2. Nonreciprocal phase response of a two-port N-path filter with phase-shifted clocks.

to their ability to implement tunable high-*Q* filters on chip without the use of inductors [28]–[30]. In this section, after recapping the principle of operation, we present detailed analyses and design considerations for this circulator. A simplified model has been used to characterize performance metrics, such as loss, isolation, linearity, and tuning range in terms of design parameters, such as number of paths and switch resistance.

A. Phase Nonreciprocity in N-Path Filters

The Faraday effect in ferrite materials produces a nonreciprocal rotation in the polarization vector of electromagnetic waves when a magnetic field bias is applied along/opposite to the direction of the propagation [31]. Analogous to this, we recently found that commutating a signal through a bank of LTI networks with staggered timing induces a nonreciprocal phase shift for signals traveling in opposite directions as these signals see a different ordering of the commutating switches [23]. The electrical implementation of the staggered commutation is a two-port N-path filter with phase-shifted clocks driving the two switch sets (Fig. 2). Through rigorous LPTV analysis for excitations at each port [23], [32], the complete S-parameters of a two-port N-path filter at the center frequency (f_s) with 90° phase shift between the clock sets [assuming $C \gg (1/(2\pi f_s Z_0))$ for filtering] can be written as

$$S(f_s) \approx \begin{bmatrix} \text{sinc}^2\left(\frac{\pi}{N}\right) - 1 & \text{sinc}^2\left(\frac{\pi}{N}\right) e^{-j\pi/2} \\ \text{sinc}^2\left(\frac{\pi}{N}\right) e^{+j\pi/2} & \text{sinc}^2\left(\frac{\pi}{N}\right) - 1 \end{bmatrix}_{N \rightarrow \infty} \approx \begin{bmatrix} 0 & e^{-j\pi/2} \\ e^{+j\pi/2} & 0 \end{bmatrix} \quad (3)$$

where N is the number of paths, C is the capacitance in each path, and Z_0 is the reference impedance. For $N \rightarrow \infty$, the N-path is simply a lossless matched nonreciprocal phase shifter.

Intuitively, the behavior can be explained using a frequency conversion and low-pass filtering analogy (Fig. 3). Each set of switches is represented by an I/Q mixer. The BB capacitances

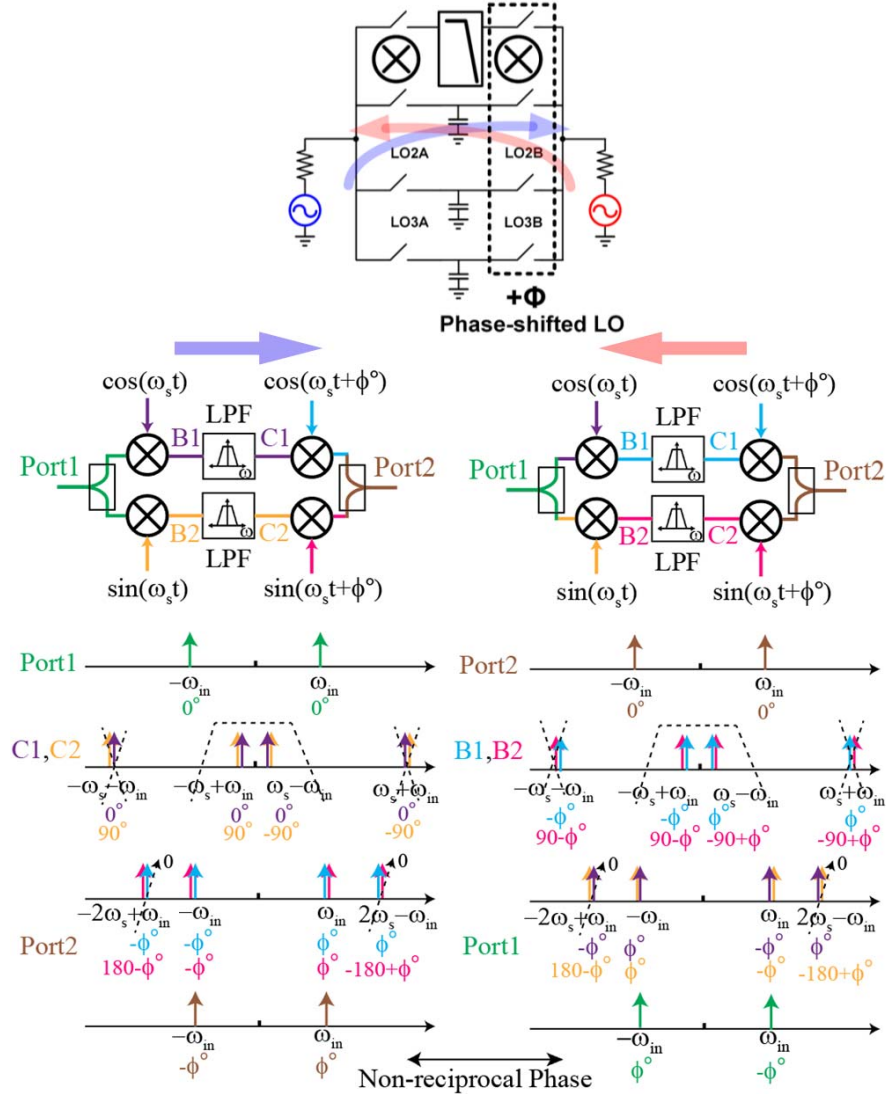


Fig. 3. Intuitive frequency conversion and filtering-based explanation of the nonreciprocal phase response of a two-port N-path filter with phase-shifted clocks.

of the N-path filter form a low-pass filter with the source and load impedances [28], filtering away the upconverted signal after the first mixing in each direction and preserving the downconverted signal, which is then upconverted back using the second set of mixers. Since the phase-shifted LO performs upconversion in one direction and downconversion in the other, nonreciprocal phase response is seen.

These S-parameters correspond to an ideal circulator with 0-dB loss and perfect matching at each port. As can be seen from (4), the voltages on either side of the N-path filter (V_x, V_y) have a magnitude of $[(\sin(\beta l)V_{in,tx})/2]$. Interestingly, by setting l to zero, the voltages across the N-path filter remain quiet for excitations at the TX port, thus enhancing the TX-ANT linearity compared with ANT-RX. Fig. 4(d) shows such a linearity-enhanced circulator where the transmission lines have been further miniaturized using lumped CLC equivalent circuits.

B. Linearity-Enhanced Circulator Topology

To create nonreciprocal wave propagation, the nonreciprocal N-path-filter with $\pm 90^\circ$ phase shift is placed inside a $3\lambda/4$

transmission line loop [Fig. 4(a)]. This results in satisfaction of the boundary condition in one direction (-270° phase shift from the loop added with -90° from the N-path filter) but not in the opposite direction ($-270^\circ + 90^\circ = -180^\circ$). As a result, waves can propagate in only one direction in the loop. In addition, a three-port circulator can be realized by placing ports anywhere along the loop as long as they maintain a $\lambda/4$ circumferential distance between them [Fig. 4(b)].

To simplify the analysis, an approximate model is shown in Fig. 4(c) in which the N-path filter is modeled with its S-parameters at the center frequency (f_s) and two series resistances (R_{sw}) representing the resistance of the switches. The behavior of an N-path filter depends on the source and load impedances, and the use of the S-parameters presented earlier that were derived with 50Ω source and load impedances represents an approximation to avoid a full-blown LPTV analysis of the entire circulator circuit.

Using conventional microwave circuit analysis techniques, 13 equations are needed to fully solve the circuit unknowns. These 13 unknowns consist of eight wave amplitudes (forward

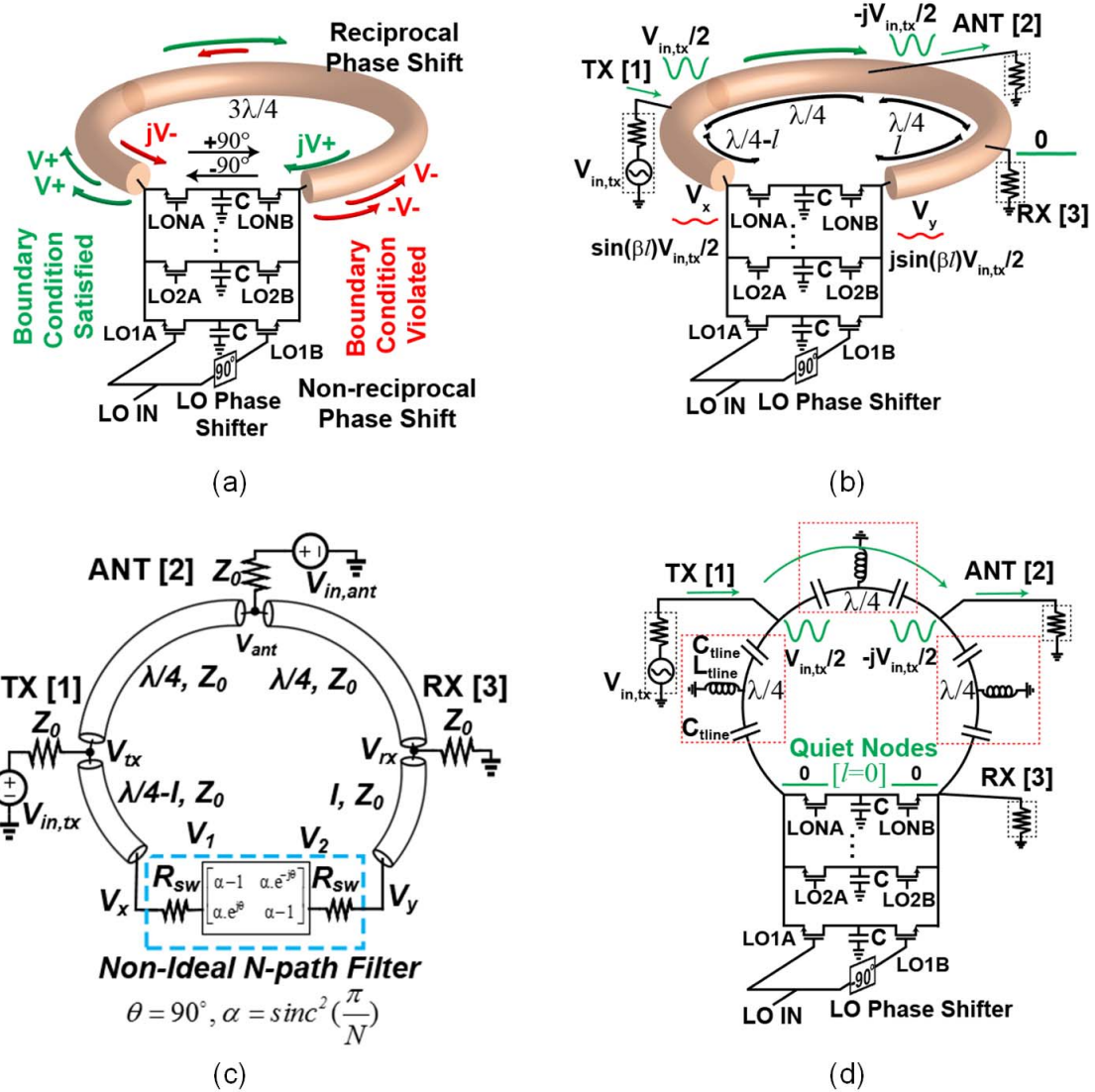


Fig. 4. (a) Nonreciprocal wave propagation achieved by placing the two-port N-path filter with $+/-90^\circ$ phase shift within a $3\lambda/4$ transmission line loop. (b) Three-port circulator structure. (c) Simplified model using the analytical S-parameters of the N-path filter and series switch resistances. (d) Miniaturized linearity-enhanced circulator constructed by placing the RX port right at the N-path filter.

and backward waves propagating in each transmission line section) and five node voltages V_{tx} , V_{ant} , V_{rx} , V_x , and V_y . For an ideal N-path filter ($N \rightarrow \infty$, $\alpha = \text{sinc}^2(\pi/N) \rightarrow 1$, $R_{sw} = 0$) and ideal lossless transmission lines, the overall S-parameters of the circulator and the port voltages for an excitation $V_{in,tx}$ at the TX port ($V_{in,ant} = 0$) are

$$V_{tx} = \frac{1}{2} V_{in,tx}, \quad V_{ant} = \frac{-j}{2} V_{in,tx}, \quad V_{rx} = 0 \\ V_x = \frac{\sin(\beta l)}{2} V_{in,tx}, \quad V_y = \frac{j \sin(\beta l)}{2} V_{in,tx} \quad (4)$$

$$S_{\text{circ}}(f_s) = \begin{bmatrix} 0 & 0 & -1 \\ -j & 0 & 0 \\ 0 & -j & 0 \end{bmatrix} \quad (5)$$

where β and l are the propagation constant of the $3\lambda/4$ ring and the distance from the RX port to the N-path filter, respectively.

C. Loss, Isolation, and Linearity Enhancement Under Nonidealities

In reality, the N-path filter is implemented using finite number of paths (N) and nonzero switch resistance (R_{sw}). In such a case, the TX-ANT loss (S_{21}) and TX-RX isolation (S_{31}) can be calculated for $l = 0$ as

$$S_{21} = \frac{-j Z_0}{Z_0 + R_{sw}} \\ S_{31} = \frac{-R_{sw} Z_0 (\frac{1}{\alpha} - 1)}{(Z_0 + R_{sw})(Z_0 + (\frac{1}{\alpha} - 1)(Z_0 + R_{sw}))}. \quad (6)$$

An equation for V_x under TX-port excitation has also been derived as follows:

$$V_x = \frac{-j R_{sw} Z_0 (2 + (\frac{1}{\alpha} - 1)(1 + \frac{2R_{sw}}{Z_0}))}{2(Z_0 + R_{sw})(Z_0 + (\frac{1}{\alpha} - 1)(Z_0 + R_{sw}))} V_{in,tx}. \quad (7)$$

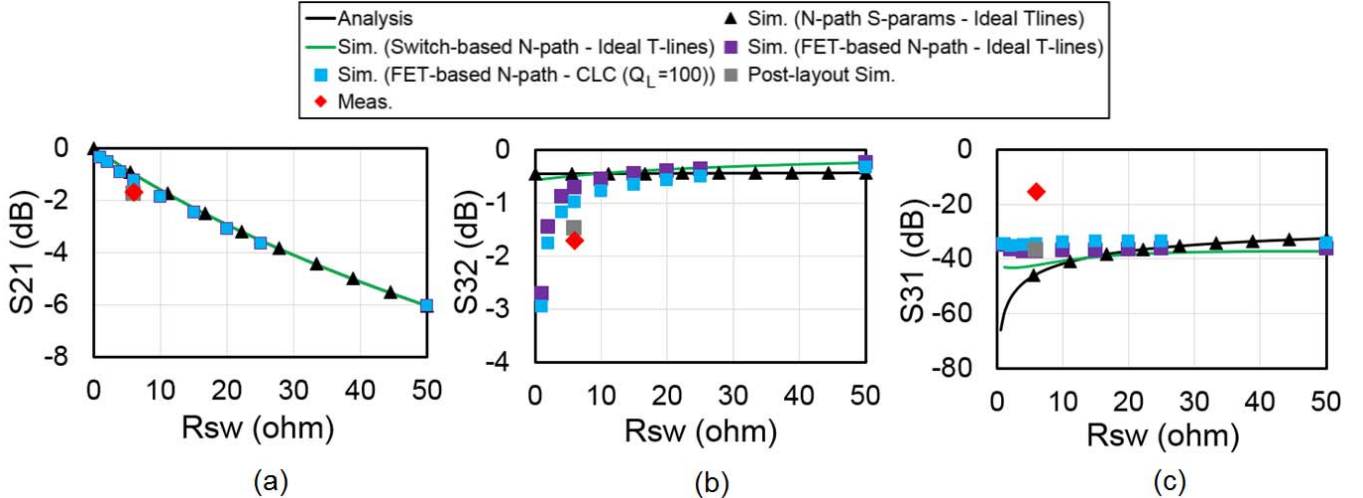


Fig. 5. Comparison of analysis, simulations (for varying complexity levels), and measured results of the circulator versus R_{sw} for $N = 8$. (a) TX-ANT loss (S_{21}). (b) ANT-RX loss (S_{32}). (c) TX-RX isolation (S_{31}).

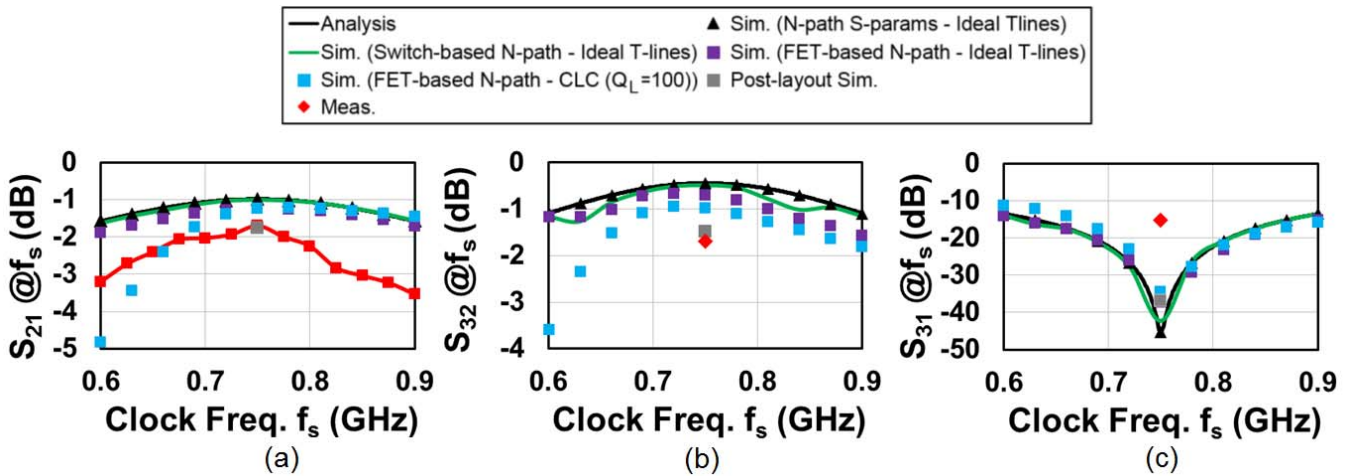


Fig. 6. Comparison of analysis, simulations (for varying complexity levels), and measured results of the circulator versus clock frequency f_s for $N = 8$ and $R_{sw} = 6 \Omega$. (a) TX-ANT loss (S_{21}) at f_s . (b) ANT-RX loss (S_{32}) at f_s . (c) TX-RX isolation (S_{31}) at f_s . The transmission lines are quarter-wave at 750 MHz.

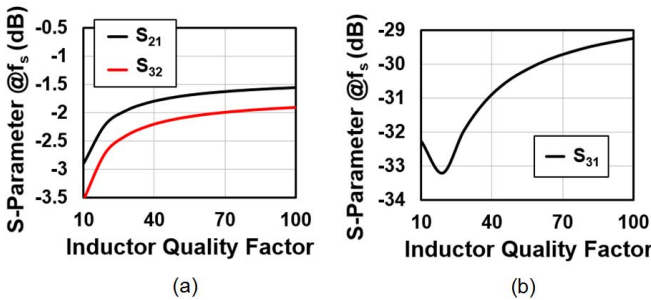


Fig. 7. Simulated effect of inductor Q on the circulator's S-parameters. (a) TX-ANT loss (S_{21}), ANT-RX loss (S_{32}), and (b) TX-RX isolation (S_{31}). Three CLC sections at 750 MHz are used with an eight-path filter employing transistor-based switches, $C_{BB} = 26 \text{ pF}$ and $R_{ON} = 6 \Omega$.

Interestingly, the TX-ANT loss is independent of N and only depends on R_{sw} , while the isolation depends on both R_{sw} and N (via α). For $N \rightarrow \infty$ ($\alpha \rightarrow 1$), the isolation becomes

perfect ($S_{31} = 0$, i.e., $V_{rx} = 0$ for TX-port excitations) and $|V_x| = |((R_{sw} V_{in,tx})/(Z_0 + R_{sw}))|$. For $R_{sw} = 0$, the isolation becomes perfect as well and $V_{rx} = V_x = 0$ for TX-port excitations.

As mentioned earlier, in the ideal scenario, the voltages across the N-path filter are quiet for TX-port excitations, and the TX linearity is enhanced substantially. When finite N and nonzero R_{sw} are considered, the linearity enhancement will be related to the finite magnitude of the voltages V_{rx} and V_x . As N is increased, the linearity enhancement is limited by the voltage swing at V_x ³. However, decreasing R_{sw} increases the linearity enhancement as both V_{rx} and V_x are suppressed.

³This scenario is similar to the out-of-band (OOB) linearity mechanism in mixer-first RXs where the voltage on one end of the N-phase mixer is nulled due to the input filtering of the transimpedance amplifier (TIA), and the voltage on the other end is limited by switch resistance.

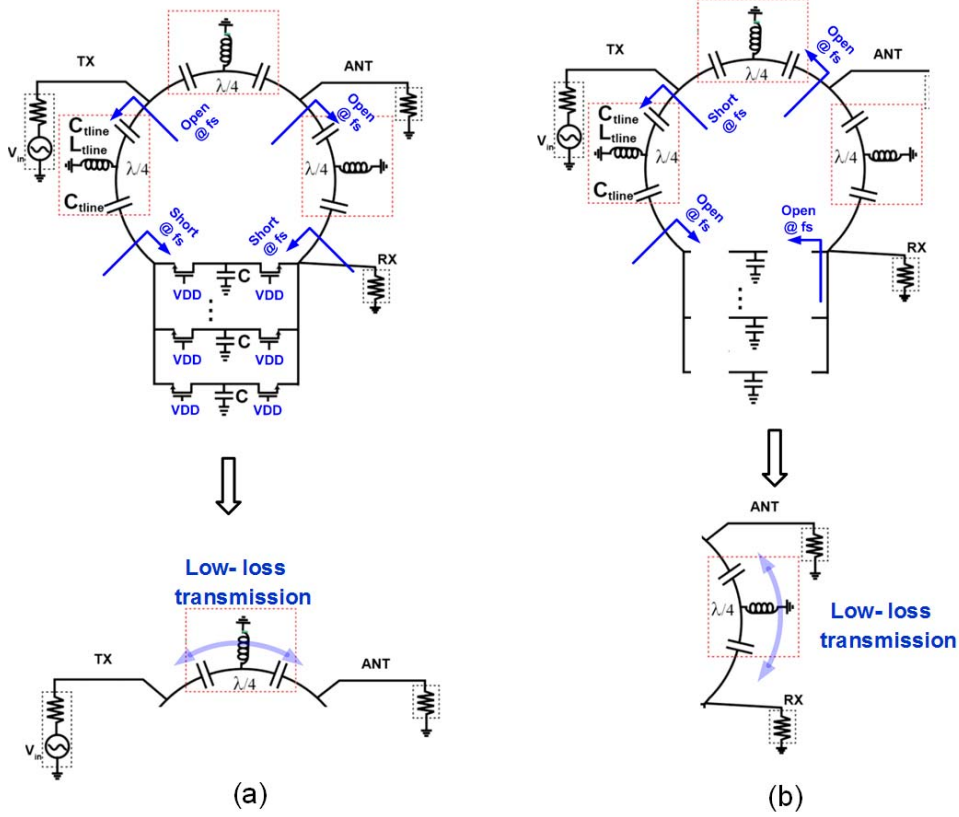


Fig. 8. TDD mode of operation. (a) TX-ANT transmission mode. (b) ANT-RX transmission mode.

Similarly, the ANT-RX loss (S_{32}) can be calculated as

$$S_{32} = \frac{-jZ_0(1 + (\frac{1}{\alpha} - 1)\frac{R_{sw}}{Z_0})}{(Z_0 + (\frac{1}{\alpha} - 1)(Z_0 + R_{sw}))}. \quad (8)$$

The ANT-RX loss depends on both R_{sw} and N . For $N \rightarrow \infty$ ($\alpha \rightarrow 1$), the ANT-RX loss becomes perfect ($S_{31} = -j$). Furthermore, for ANT port excitations, the voltages on both sides of the N-path filter have the same magnitude ($|V_x| = |V_{rx}| = |((S_{32})/(2V_{in,ant}))|$). In other words, the ANT excitation appears in common mode across the N-path filter. Due to this fact, the IB ANT-RX linearity is identical to the linearity of the N-path filter.

Fig. 5 shows calculations, simulations (at varying levels of complexity), and measured performance as a function of R_{sw} for $N = 8$. As can be seen in Fig. 5(a), the analysis closely predicts the TX-ANT loss (S_{21}). A good agreement is seen in ANT-RX loss (S_{32}) as well, although the simulated (with real FETs) and measured loss values increase beyond the theory for larger switch sizes (lower R_{sw}) due to the increase in the parasitic capacitance directly in parallel with the RX port. These effects would be exacerbated for higher operating frequencies, but would be alleviated through use of more scaled CMOS technology nodes at the potential expense of the power handling. As such, using currently available CMOS technologies, this circulator concept is viable at RF frequencies where N-path filters have been explored. TX-RX isolation (S_{31}) is predicted to improve for larger switch sizes, becoming perfect at $R_{sw} = 0$ as discussed earlier. The simulated (with real FETs) and

measured TX-RX isolations are also lower than analysis for lower R_{sw} values due to small mismatches produced by capacitive parasitics, necessitating an antenna impedance tuner (as is the case with all circulators).

D. Tuning Range of the Circulator

While the N-path filter can be tuned by changing the clock frequency, the tuning range of the circulator is limited by the use of quarter-wave transmission lines (or their equivalents). Similar to Section III-C, the tuning range of the circulator can be derived using the model shown in Fig. 4(c). The analysis has been performed for the general case when the transmission lines are not quarter wavelength, with both switch resistance R_{sw} and finite number of paths N considered. The closed form expressions for S_{21} , S_{32} , and S_{31} at f_s as f_s is tuned are complex and have been presented in the Appendix.

Fig. 6 shows calculations, simulations (at varying levels of complexity as before), and measurement results of the insertion losses and TX-RX isolation as a function of clock frequency f_s . Each transmission line is quarter wave at 750 MHz, $R_{sw} = 6\Omega$, and $N = 8$. Fig. 6(a) and (b) shows the TX-ANT loss (S_{21}) and ANT-RX loss (S_{32}), confirming that the analysis can predict the loss closely even for the case when an FET-based N-path filter is used. The use of CLC equivalents as opposed to a true quarter-wave transmission line results in an increase in loss as the circulator is tuned, which is the price to be paid for miniaturization. Nevertheless, it can be seen from Fig. 6(a) and (b) that S_{21} and S_{32} can remain low for as high as 30% tuning around the center frequency. On the

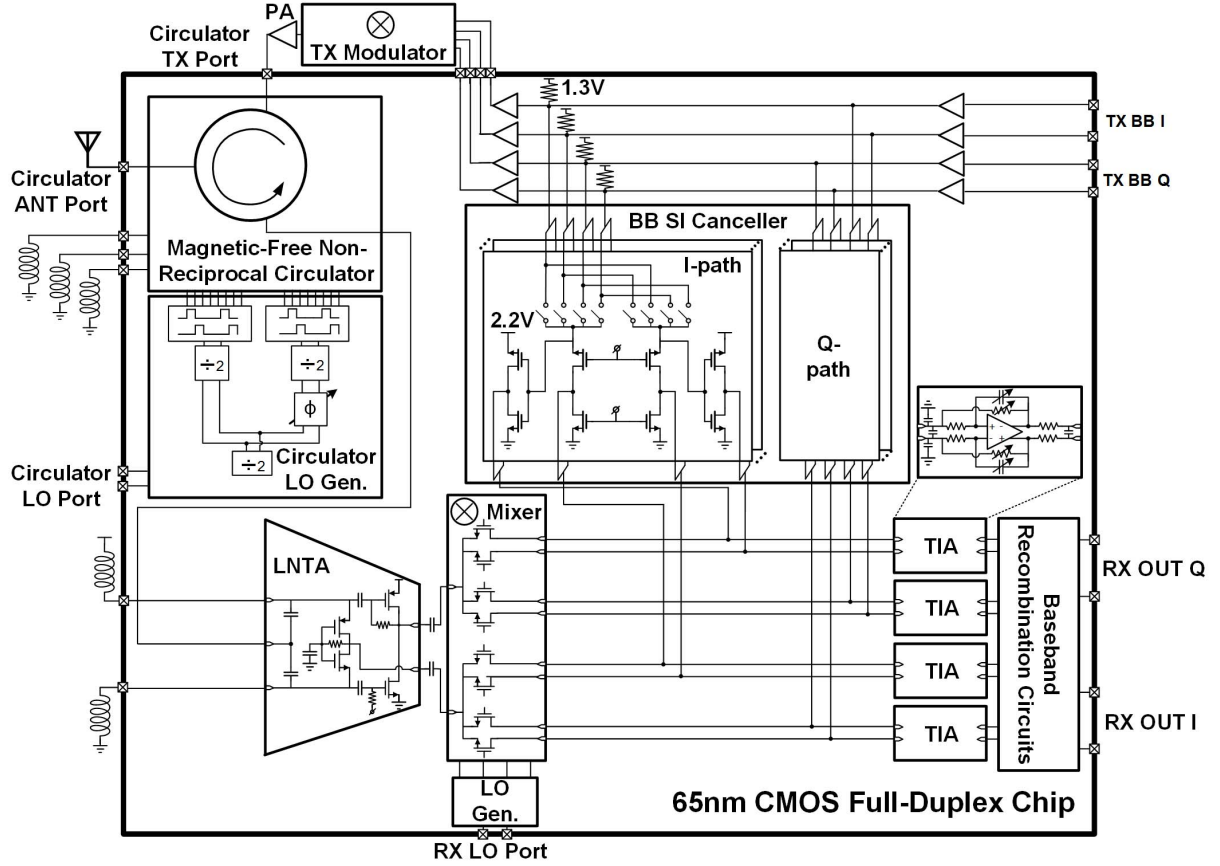


Fig. 9. Block diagram and schematic of the implemented 65-nm CMOS FD RX with integrated circulator and analog BB SI cancellation.

other hand, Fig. 6(c) shows the sensitivity of the isolation to frequency tuning, necessitating an antenna port impedance tuner as is the case with all circulators.

E. Effect of Inductor Quality Factor

Fig. 7 shows simulated circulator loss and isolation as the inductor quality factor is varied. The simulation setup consists of three CLC sections, each designed to emulate a quarter-wave transmission line at 750 MHz using ideal capacitors and inductors with a resistor in series with the inductor. An eight-path filter is used with transistor-based switches, $C_{BB} = 26 \text{ pF}$ and $R_{ON} = 6\Omega$, similar to our implementation. As expected, lowering the inductor Q increases the losses in both TX-ANT and ANT-RX paths. The losses are lower than 2.5 dB for Q values of 25 and higher, which is achievable using integrated passive device technologies.

In addition, the isolation is not significantly affected by the inductor Q , and even initially improves, since the losses through the transmission line match that of the N-path filter. In a practical scenario, as mentioned earlier, the isolation will be limited by parasitics and antenna mismatch, necessitating an antenna port impedance tuner as is the case with all circulators.

F. TDD Mode of Operation

The circulator can also be configured to operate as a reciprocal T/R switch for half-duplex TDD applications. For TX-ANT transmission, the switches of at least one path need

to be turned on permanently, creating a virtual ground at the RX port due to the large capacitance in parallel. This low impedance is transformed to relatively high impedances at the TX and ANT ports by the two quarter-wavelength transmission lines on each side of the N-path filter. Hence, the circuit simplifies to a low-loss $50\text{-}\Omega$ t-line between TX and ANT [Fig. 8(a)]. Similarly, if all the switches of the N-path filter are turned off, the high impedance at the N-path filter is transformed to a low impedance at the TX port, which, in turn, is transformed to a high impedance at the ANT port. The resulting equivalent circuit is a low-loss $50\text{-}\Omega$ t-line between ANT and RX [Fig. 8(b)]. It should be noted, however, that the circulator prototype described later in this paper was not optimized to achieve high TX-RX isolation in this reciprocal T/R switch mode of operation.

IV. IMPLEMENTATION

A. Integrated Circulator

A standalone circulator was designed for tunable operation around 750 MHz in 65-nm CMOS. The schematic of the circulator is shown in Fig. 4(d). The $(3\lambda/4)$ line is miniaturized using three CLC sections implemented with on-chip MiM capacitors and off-chip air-core 8.9-nH inductors (0806SQ from Coilcraft, $Q_L > 100$). The N-path filter uses eight paths to reduce S_{32} losses. The capacitance of each path is 26 pF, chosen for 30-MHz ANT-RX BW. Switch resistance for each of the sixteen transistors is 6Ω , determined based

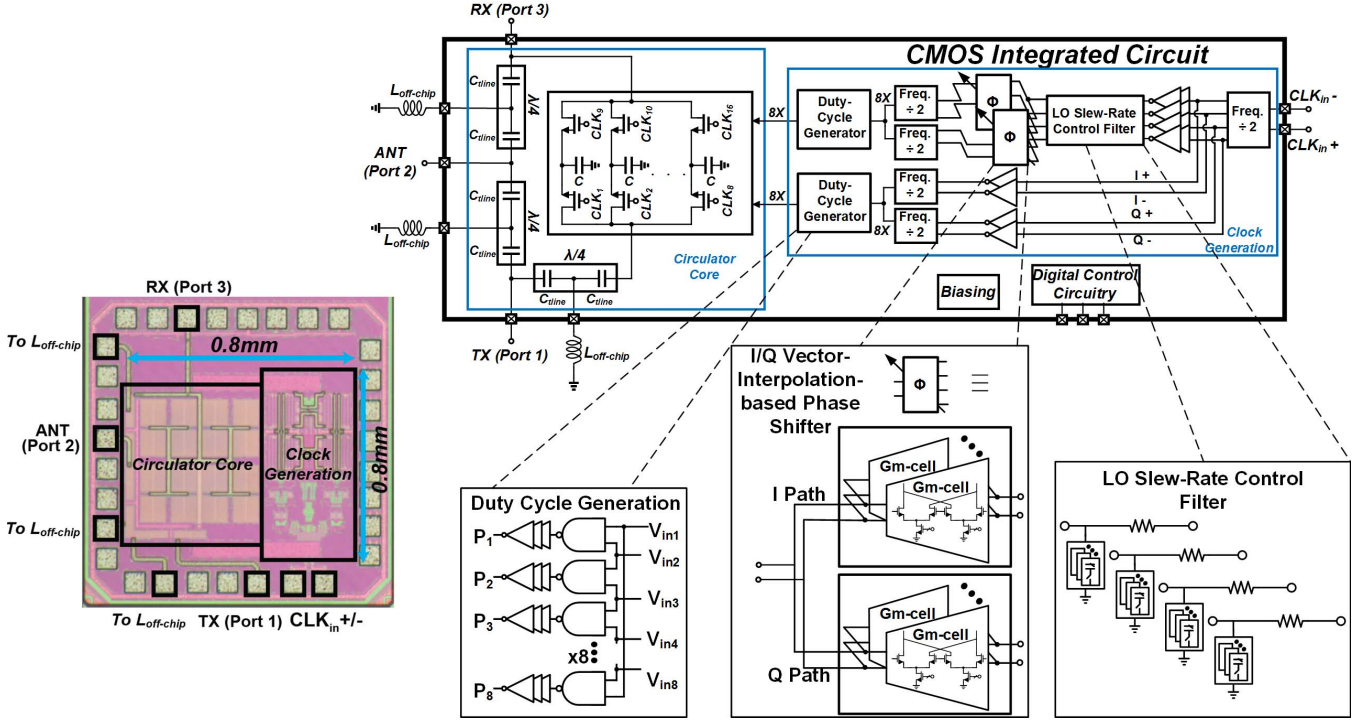


Fig. 10. Chip microphotograph of the standalone 65-nm CMOS nonreciprocal N-path-filter-based passive circulator along with the detailed block and circuit diagrams of the LO path.

on the S_{21} - S_{32} tradeoff and to maximize TX-ANT linearity performance. Clock phase shifting is accomplished using four-phase vector-interpolation phase shifters at twice the switching frequency, followed by a second frequency division to achieve eight phases. The detailed LO path block and circuit diagrams can be found in Fig. 10.

B. Integrated Receiver and Analog Baseband SI Canceller

The circulator is integrated with a noise-canceling current-mode RX (see Fig. 9). Both the circulator and the RX are powered from 1.2-V supplies. The noise-canceling current-mode RX, similar to that in [11], consists of a common-gate (CG), common-source (CS) low-noise transconductance amplifier (LNTA), four-phase passive mixers, TIAs, and analog BB recombination circuitry. SIC at the analog BB is required to further relax the RX and ADC DR requirements as discussed in Section II. The analog BB canceller taps from the TX BB, adjusts the amplitude and the phase, and injects the cancellation current at the TIA input. Performing BB SIC at the TIA input not only protects the RX analog BB circuits, but also enhances the RX mixer and LNTA linearity by creating a virtual ground at the passive mixer output. Amplitude and phase scaling are achieved through two 5-b digitally controlled phase rotators injecting into the I- and Q-paths of the RX analog BB. Each phase rotator consists of 31 identical cells with independent controls, similar to [5]. The unit cell of the phase rotator adopts a noise-canceling CG and CS topology, allowing partial cancellation of the noise from the CG devices (dependent on the phase rotator setting); 1.3- and 2.2-V supplies are used for the BB canceller as indicated in Fig. 9.

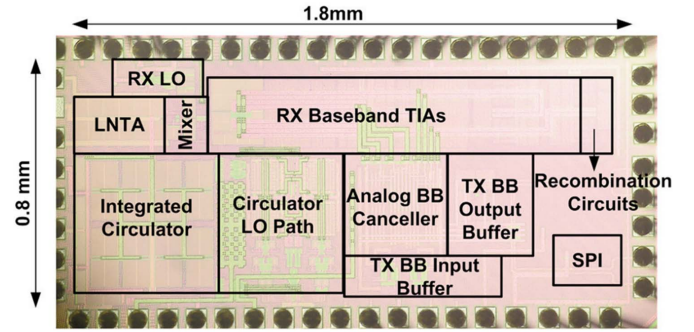


Fig. 11. Chip microphotograph of the 65-nm CMOS FD RX with integrated circulator and analog BB SI cancellation.

V. MEASUREMENT RESULTS

The chip microphotograph of the 65-nm CMOS circulator is shown in Fig. 10. The circulator has an active area of 0.64 mm² and is mounted in a QFN24 package. The chip microphotograph of the 65-nm CMOS SI-canceling FD RX with the integrated circulator is shown in Fig. 11. The chip has an active area of 1.44 mm² and is mounted in a QFN56 package.

A. Integrated Circulator

The measured S-parameters of the circulator for a clock frequency of 750 MHz are shown in Fig. 12 for two cases: first, when all ports are terminated with $50\ \Omega$, and second, when the third port is slightly tuned using an off-chip impedance tuner

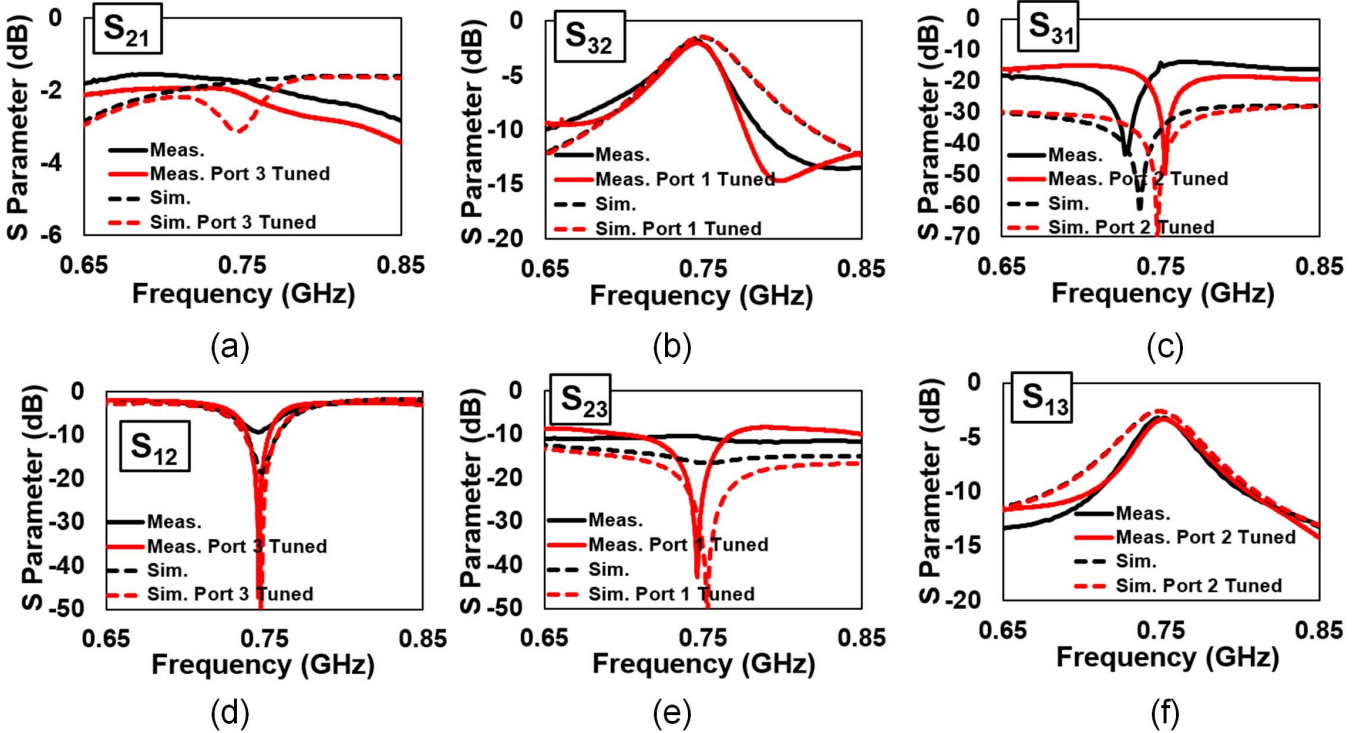


Fig. 12. Circulator S-parameter measurements and simulation results for a clock frequency of 750 MHz. (a) S_{21} . (b) S_{12} . (c) S_{32} . (d) S_{23} . (e) S_{31} . (f) S_{13} . The measurements and simulations have been done for two cases: first, when all ports are terminated with $50\ \Omega$, and second, when the third port is slightly tuned to maximize the reverse isolation at the center frequency.

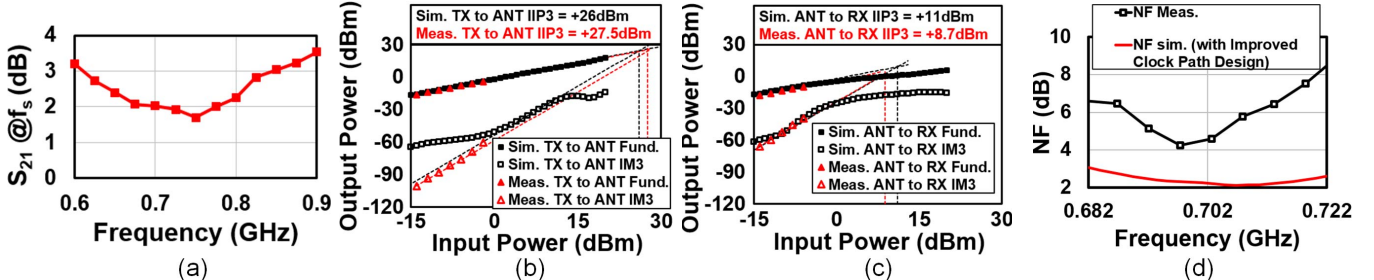


Fig. 13. (a) Measured TX-ANT loss at the center frequency as clock frequency is tuned. Phase tuning is used at each frequency to ensure minimum loss. Simulated and measured IB IIP3 of (b) TX-ANT path and (c) ANT-RX path. (d) Measured and simulated ANT-RX NF of the circulator for a clock frequency of 700 MHz.

to maximize the reverse isolation at the center frequency⁴. The TX-ANT path has a wideband response and exhibits 1.7 dB of loss at the center frequency. The ANT-RX path experiences the filtering profile of the N-path filter, with a minimum loss of 1.7 dB at the center frequency. The circulator has broadband TX-RX isolation better than 15 dB. By slightly tuning the ANT impedance, it achieves narrowband isolation of up to 50- and 20-dB isolation BW of 32 MHz. An excellent correlation to simulations is also seen. In addition, in the TDD operation modes, the losses are 1.8 and 1 dB for TX-ANT and ANT-RX paths, respectively. Fig. 13(a) shows the TX-ANT loss at the center frequency as clock frequency is tuned. For each clock frequency, phase-shift tuning between the clocks on either side is used to minimize the losses. Less than 3-dB loss is maintained over 610–850 MHz.

⁴It should be noted that all circulators in general require an impedance tuner as the TX-to-RX isolation is extremely sensitive to reflections at the ANT port.

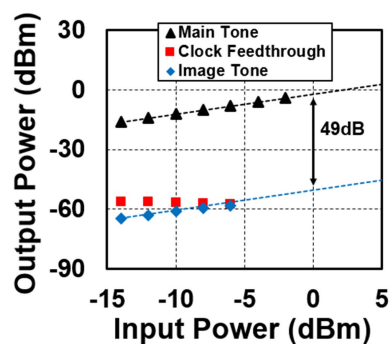


Fig. 14. Measured clock feedthrough to the ANT port and IQ image rejection for TX-ANT transmission. The swept-power TX tone is at 748 MHz and a clock frequency of 750 MHz is used.

The measured circulator IB TX-ANT IIP3 is +27.5 dBm while the ANT-RX IB IIP3 is +8.7 dBm [Fig. 13(b) and (c)], a remarkable ≈ 20 -dB improvement due to the linearity enhancement technique (i.e., $l = 0$). A good agreement with

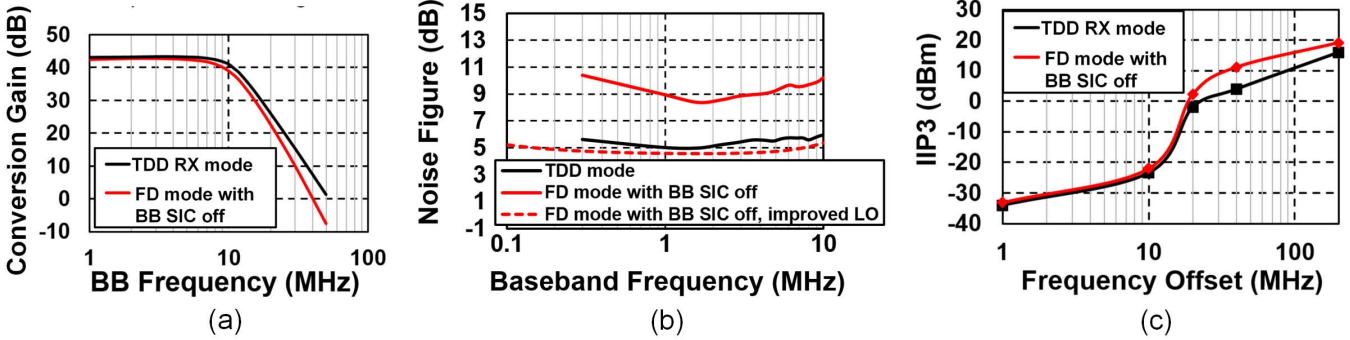


Fig. 15. Measured FD RX ANT-to-RX-BB characteristics. (a) Conversion gain. (b) Noise figure. (c) IIP3.

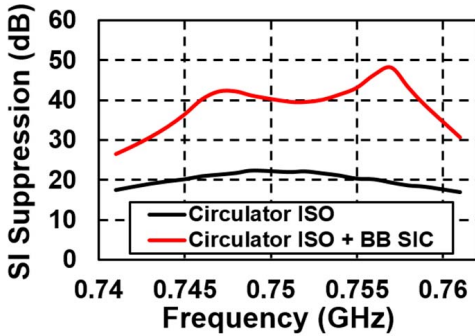


Fig. 16. Measured small-signal SI suppression across the circulator and analog domains using a joint-SIC approach.

simulations is also seen. These linearity simulations employ the approach described in [33] to combat BSIM's modeling deficiencies. The measured ANT-RX NF is 4.3 dB, as shown in Fig. 13(d). This NF is higher than the ANT-RX loss, and is degraded by 2.3 dB when compared with the simulated NF with ideal clocks due to the implementation approach of the clock phase shifter (the square-wave digital clocks are attenuated and filtered to produce weak sine waves for linear vector interpolation as shown in Fig. 10, leading to susceptibility to phase noise). Simulations reveal that usage of static 90° phase shifts or digital phase interpolators that preserve the square-wave nature of the clock in an improved clock path design lowers the NF to the expected 2-dB value. Retiming the multiple phases with the original LO signal has also been shown to be beneficial in prior art [29]. Quantifying the impact of LO phase noise on circulator NF, particularly in the presence of TX SI, is a topic for future research. Fig. 14 shows measurements that reveal a clock feedthrough to the ANT port of about -57 dBm at the center frequency and an IQ image rejection of 49 dB for TX-ANT transmission.

B. Receiver With Circulator

The SI-canceling FD RX with the integrated circulator operates over 610–850 MHz, with peak gain of 42 dB, IB IIP3 of -33 dBm at peak gain, and OOB IIP3 of $+19$ dBm at 200-MHz offset and $+11$ dBm at 40-MHz offset when the circulator is in FD mode (Fig. 15). All these results are referred to the ANT port. When the circulator is configured in TDD mode, the measured peak gain and IB IIP3 at peak gain are the same as when the circulator is in FD mode. The measured OOB IIP3 is $+16$ dBm at 200-MHz offset and $+4$ dBm at

40-MHz offset. The OOB IIP3 in FD mode benefits from the filtering effect of the circulator's N-path filter at the RX input. The measured NF is 5.0 dB in TDD RX mode, and increases to 8.4 dB in FD mode due to the circulator LO path phase noise issue described earlier [as in Fig. 15(b)]. The improved LO design described earlier restores the FD mode NF to 5 dB in simulation.

C. Transmitter and LO Path for FD Measurements

The TX uses an off-the-shelf quadrature modulator from TI (TRF370417) that is driven by the integrated TX BB buffers, and has a measured output IP3 of $+20$ dBm. The TX output noise level is measured to be -145 dBm/Hz. Given 20-dB circulator isolation, the TX noise floor at the RX input would be -165 dBm/Hz, which is 3 dB lower than the RX input-referred noise floor. The measured TX image rejection ratio is greater than 30 dB, and thus does not limit the targeted 20-dB analog BB SIC.

The circulator and the FD RX receive clock inputs at four times and twice the RF carrier frequency, respectively. In the measurement, a custom-designed discrete-component-based divide-by-two divider was used in the RX LO path allowing the circulator and the FD RX to share one LO source. The TX modulator, which receives an LO at the RF carrier frequency used a separate LO source. Thanks to a relatively low TX output power level and the fact that we used high-quality signal sources, the noise floor induced by the lack of correlation between TX and RX phase noise does not degrade the original noise floor of the RX.

D. Full-Duplex Operation

A joint-SIC approach was used for achieving better overall SIC across the circulator and analog domains. Given the frequency-flat amplitude- and phase-based analog canceller, maximizing the circulator TX-RX isolation at a single frequency by tuning the ANT impedance (see Fig. 12) is not optimal for overall SIC. The antenna tuning was optimized to get a flat isolation of about 20 dB from the circulator (see Fig. 16), allowing better SIC from the subsequent analog BB canceller. In the measurement, an average overall SI suppression of 42 dB was achieved across the circulator and analog BB canceller over a BW of 12 MHz (Fig. 16).

As shown in Fig. 17, the analog BB SI canceller further increases the RX NF to 10.9 dB (TX signal not present). With the improved LO design for the circulator as described earlier,

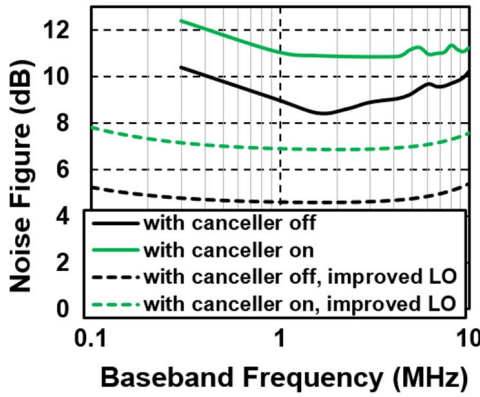


Fig. 17. Measured and simulated (with an improved circulator LO design) impact of the analog BB SI canceller on RX NF in the FD mode.

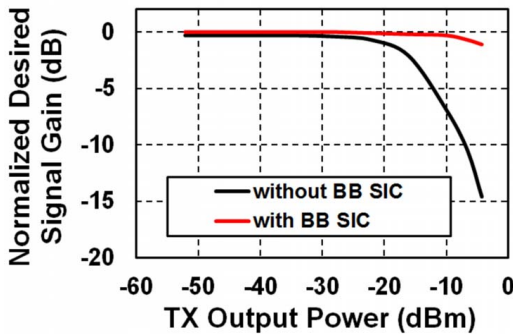


Fig. 18. Measured ANT-to-RX-BB gain compression of a weak desired signal with and without analog BB SIC versus varying TX output power level.

a 7-dB NF with canceller on is obtained in simulation. Fig. 18 shows linearity tests under powerful SI with the same antenna tuning mentioned before for 42-dB average overall SIC. SIC of up to -4 dBm of TX power results in small gain compression (1 dB) of a desired signal, as opposed to nearly 15 dB of compression in the absence of analog BB SIC.

Fig. 19(b) shows both the main two-tone SI at the RX output as well as IM3 distortion generated on the SI by the circulator, RX and BB canceller for varying TX two-tone power. All signals are referred back to the ANT port to enable comparison with the noise floor of -92 dBm. The same antenna tuning that was applied in the joint-SIC approach is used here. Analog BB SIC improves the effective IB RX IIP3 from -33 to -18 dBm. We have also implemented digital SIC in MATLAB after capturing the BB signals using an oscilloscope (an 8-b quantizer). The digital SIC is based on a nonlinear tapped delay line [see Fig. 19(a)], which essentially models the SI channel in digital as a truncated Volterra series

$$y[n] = \sum_{k=0}^N h_1[k]x[n-k] + \sum_{k=0}^N h_2[k]x^2[n-k] + \sum_{k=0}^N h_3[k]x^3[n-k] + \dots + \sum_{k=0}^N h_p[k]x^p[n-k] \quad (17)$$

where $y[n]$ is the nonlinear tapped delay line output for SIC, $x[n]$ and $x[n-k]$ (k represents the delay index) are the current and past TX digital BB signals, N corresponds to the maximum delay in the modeled SI channel, and

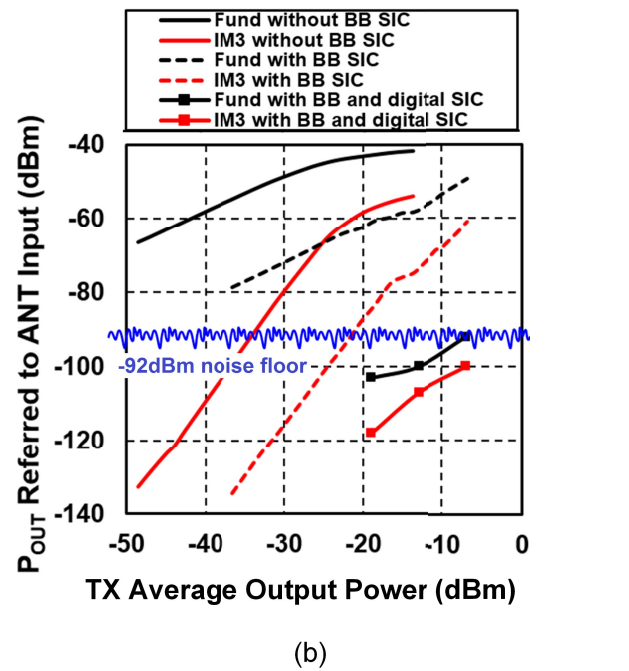
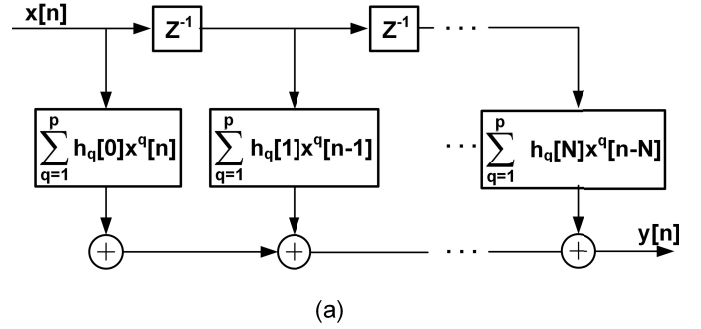


Fig. 19. (a) Nonlinear tapped delay line used for digital SIC and (b) measured two-tone linearity test with SI suppression across antenna, analog BB, and digital domains.

$h_i[k]$ ($i = 1, 2, 3, \dots, p$) is the i th-order digital canceller coefficient for a delay index of k . The truncation of the Volterra series helps to reduce the digital SI canceller complexity to a manageable level. In our measurement, nonlinear terms up to fourth order are considered (i.e., $p = 4$) with a delay spread length of 41 samples, resulting in 164 total unknown canceller coefficients. The digital SI canceller coefficients are determined using a two-tone pilot signal. By considering both the delay spread and the nonlinearities of the SI channel, the digital SIC cancels not only the main SI but also the IM3 distortion generated on the SI. After digital SIC, the main SI tones are at the noise floor, while the SI IM3 tones are 8 dB below for -7 -dBm TX average power. This corresponds to a total SI suppression of 85 dB. As can be seen here, the -7 -dBm TX average power is not limited by the power handling of the circulator, but rather by the need to cancel the main SI down to the noise floor in this measurement (in other words, by the achieved total SI suppression).

Table III compares this paper to prior integrated FD RXs. The novel aspects of this paper include the integrated nonmagnetic nonreciprocal passive circulator with very low TX-ANT

TABLE III
PERFORMANCE SUMMARY AND COMPARISON

| | JSSC 2015 [11] | JSSC 2015 [5] | JSSC 2015 [6] | This work |
|--|--|--|--|--|
| Architecture | RX with wideband SIC based on RF frequency-domain equalization | Mixer-first RX with SI-cancelling VM-downmixer | Mixer-first TRX with Active Baseband Duplexing | RX with integrated magnetic-free N-path-filter-based circulator and BB SIC |
| RX Frequency | 0.8-1.4 GHz | 0.15-3.5 GHz | 0.1-1.5 GHz | 0.6-0.8 GHz |
| Maximum Gain | 42 dB | 24 dB | 53 dB | 42 dB |
| Noise Figure | 4.8 dB | 6.3 dB | 5-8 dB | 5.0 dB (TDD mode) |
| OOB IIP3 | +17 dBm | +22.0 dBm | +22.5 dBm | +19 dBm |
| IB IIP3 | -20 dBm at 27 dB gain | +9 / +19 dBm at 24dB gain (Neg. conductance off/on) | -38.7 dBm at 53 dB gain | -33 dBm at 42 dB gain |
| Integrated Antenna Interface | No | No | Yes (baseband duplexing LNA) | Yes (magnetic-free non-reciprocal circulator) |
| Integrated SI Suppression Domains | RF | RF | Analog BB | Antenna + Analog BB |
| Amount of Integrated SI Suppression | 20 dB SIC across 25 MHz BW | 21 dB integrated SIC across ~16 MHz BW | 33 dB across 300kHz TX BB BW | 42 dB SIC across 12 MHz BW (incl. integrated circulator) |
| Effective IIP3 with respect to RX/ANT Input | +2 dBm at 27 dB gain | +21.5 dBm at 24dB gain | N/A | -18 dBm at 42 dB gain |
| Effective IIP3 with respect to TX Power | N/A | N/A | -0 dBm at 43/53 dB gain ¹ | +1 dBm at 42 dB gain |
| NF Degradation in Full-Duplex Mode | 0.9/1.3 dB ⁴ | 4-6 dB ⁵ | N/R | 5.9 dB ² (incl. circulator in FD mode) |
| Overall SI Suppression | 56 dB (incl. 34 dB isolation from antenna pair) | 46 dB (incl. 25 dB isolation from antenna pair) | N/A | 85 dB (incl. digital SIC) |
| RX Power | 63-69 mW | 22-46 mW | 43-56 mW (incl. TX) | 60 mW signal path + 10 mW LO path (at 0.7GHz) |
| SI Canceller Power | 0-182 mW | 1-10 mW | | 30 mW |
| Antenna Interface Power | N/A | N/A | N/A | 59mW ³ (at 0.7GHz) |
| Technology | 65 nm CMOS | 65 nm CMOS | 65 nm CMOS | 65 nm CMOS |
| Active Area | 4.8 mm ² | 2 mm ² | 1.5 mm ² | 1.4 mm ² |

1. From Fig. 31(a) in the paper. 2. Includes circulator 4.3dB NF, which is degraded from the expected 2dB NF due to LO phase noise. Elimination of the phase shifters (not necessary as only a static 90°phase shift is desired) restores the circulator NF to 2dB in simulation.

3. Circulator power consumption can be significantly reduced if the phase shifters are removed as only a static 90°phase shift is desired.

4. One/two canceller filters enabled. 5. Across VM settings.

N/A: Not Applicable N/R: Not Reported

loss (1.7 dB) and 85-dB total SI suppression in conjunction with digital SIC.

VI. CONCLUSION

We have demonstrated the first nonmagnetic nonreciprocal passive CMOS circulator based on N-path filter concepts, with low loss, high isolation, and enhanced linearity to the TX port. Furthermore, an SI-canceling (SIC) FD RX with the proposed integrated circulator and analog BB SIC is presented that achieves 42-dB on-chip SI suppression across the circulator and analog BB domains over a 12-MHz signal BW using a joint-SIC approach. In conjunction with digital SI and its IM3 distortion cancellation, the FD RX demonstrates 85-dB overall SI suppression, enabling an FD link budget of -7 dBm

TX average output power and -92-dBm noise floor. Topics for future research include further enhancing the TX power handling of the circulator and FD RX, further increasing circulator isolation BW and overall SI suppression BW, incorporation of low-loss antenna tuning functionality within the circulator structure (similar to electrical-balance duplexers), and understanding the harmonic response of the circulator, particularly in the presence of miniaturized CLC sections, and suppression of the same.

APPENDIX

Let us define (10) and (11), shown at the bottom of this page.

$$A = \frac{je^{j\beta l}(2 + (\frac{1}{\alpha} - 1)\frac{2R_{sw}}{Z_0} + \frac{Z_0}{R_{sw}}\sin(\beta l)) + \sin(\beta l)(-\frac{Z_0}{R_{sw}} - 2(\frac{1}{\alpha} - 1) + j\frac{Z_0}{R_{sw}}\cos(\beta l))}{e^{j\beta l}(j + \cos(\beta l) + j\frac{Z_0}{R_{sw}}\sin(\beta l)) + \sin(\beta l)(-\frac{Z_0}{R_{sw}} - \sin(\beta l) + j\frac{Z_0}{R_{sw}}\cos(\beta l))} \quad (10)$$

$$B = \frac{1}{e^{j\beta l}[j(2 - A + (\frac{1}{\alpha} - 1)\frac{2R_{sw}}{Z_0}) + \cos(\beta l)(2A + (A - 1)\frac{Z_0}{R_{sw}}) + \sin(\beta l)(2j\frac{Z_0}{R_{sw}}(A - 1) + jA)] + j\cos(\beta l)(\frac{Z_0}{R_{sw}}(1 - A) + 2(\frac{1}{\alpha} - 1))} \quad (11)$$

$$C = \frac{-je^{j\beta l}(2 + (\frac{1}{\alpha} - 1)\frac{2R_{sw}}{Z_0})\cos(\beta l) - 2j(\frac{Z_0}{2R_{sw}} + (\frac{1}{\alpha} - 1))\cos^2(\beta l) + j\frac{Z_0}{R_{sw}}\sin(\beta l) + 2je^{2j\beta l}(2 + \frac{Z_0}{2R_{sw}} + (\frac{1}{\alpha} - 1)(1 + \frac{2R_{sw}}{Z_0}))}{\cos(\beta l)(1 - je^{j\beta l} - j\frac{Z_0}{R_{sw}}\cos(\beta l)) + j\frac{Z_0}{R_{sw}}\sin(\beta l) + 2je^{2j\beta l}(1 + \frac{Z_0}{2R_{sw}})} \quad (13)$$

$$D = \frac{1}{j(2 - C + (\frac{1}{\alpha} - 1)\frac{2R_{sw}}{Z_0}) + 3(C(\cos(\beta l) + j\frac{Z_0}{R_{sw}}\sin(\beta l)) - j\frac{Z_0}{R_{sw}}\sin(\beta l) - e^{-j\beta l}(-j\cos(\beta l)(\frac{Z_0}{R_{sw}}(C - 1) - 2(\frac{1}{\alpha} - 1)) + ((1 - \frac{Z_0}{R_{sw}})C + \frac{Z_0}{R_{sw}})))} \quad (14)$$

$$S_{21}(f_s) = D \left[je^{j\beta l} \left(-C + 2 + \left(\frac{1}{\alpha} - 1 \right) \frac{2R_{sw}}{Z_0} \right) + \sin(\beta l) \left(C \frac{Z_0}{R_{sw}} + j \frac{Z_0}{R_{sw}} + 2j \left(\frac{1}{\alpha} - 1 \right) \right) \right] \quad (15)$$

$$S_{31}(f_s) = jD \left(-2C + 4 \left(1 + \frac{R_{sw}}{Z_0} \left(\frac{1}{\alpha} - 1 \right) \right) \right) \quad (16)$$

The ANT-RX insertion loss (S_{32}) at the center frequency as f_s is tuned is given by

$$S_{32}(f_s) = 2B \left(-jA + 2j \left(1 + \frac{R_{sw}}{Z_0} \left(\frac{1}{\alpha} - 1 \right) \right) \right) \quad (12)$$

where l is the quarter wavelength of the transmission lines and β is the phase constant at f_s . Similarly, the TX-ANT insertion loss (S_{21}) and TX-RX isolation (S_{31}) as the clock frequency is tuned are given by (13)–(16), shown at the top of this page.

REFERENCES

- [1] D. Bharadia, E. McMillin, and S. Katti, “Full duplex radios,” in *Proc. ACM SIGCOMM*, 2013, pp. 375–386.
- [2] A. Sabharwal, P. Schniter, D. Guo, D. W. Bliss, S. Rangarajan, and R. Wichman, “In-band full-duplex wireless: Challenges and opportunities,” *IEEE J. Sel. Areas Commun.*, vol. 32, no. 9, pp. 1637–1652, Sep. 2014.
- [3] S. Hong *et al.*, “Applications of self-interference cancellation in 5G and beyond,” *IEEE Commun. Mag.*, vol. 52, no. 2, pp. 114–121, Feb. 2014.
- [4] J. Marasevic, J. Zhou, H. Krishnaswamy, Y. Zhong, and G. Zussman, “Resource allocation and rate gains in practical full-duplex systems,” in *Proc. ACM SIGMETRICS*, Jun. 2015, pp. 109–122.
- [5] D. J. van den Broek, E. A. M. Klumperink, and B. Nauta, “An in-band full-duplex radio receiver with a passive vector modulator downmixer for self-interference cancellation,” *IEEE J. Solid-State Circuits*, vol. 50, no. 12, pp. 3003–3014, Dec. 2015.
- [6] D. Yang, H. Yüksel, and A. Molnar, “A wideband highly integrated and widely tunable transceiver for in-band full-duplex communication,” *IEEE J. Solid-State Circuits*, vol. 50, no. 5, pp. 1189–1202, May 2015.
- [7] J. Zhou, N. Reiskarimian, and H. Krishnaswamy, “Receiver with integrated magnetic-free N-path-filter-based non-reciprocal circulator and baseband self-interference cancellation for full-duplex wireless,” in *IEEE Int. Solid-State Circuits Conf. (ISSCC) Dig. Tech. Papers*, Jan. 2016, pp. 178–180.
- [8] T. Dinc, A. Chakrabarti, and H. Krishnaswamy, “A 60 GHz same-channel full-duplex CMOS transceiver and link based on reconfigurable polarization-based antenna cancellation,” in *Proc. IEEE Radio Freq. Integr. Circuits Symp. (RFIC)*, May 2015, pp. 31–34.
- [9] T. Dinc and H. Krishnaswamy, “A T/R antenna pair with polarization-based reconfigurable wideband self-interference cancellation for simultaneous transmit and receive,” in *IEEE MTT-S Int. Microw. Symp. Dig.*, May 2015, pp. 1–4.
- [10] J. Zhou, A. Chakrabarti, P. R. Kinget, and H. Krishnaswamy, “Low-noise active cancellation of transmitter leakage and transmitter noise in broadband wireless receivers for FDD/co-existence,” *IEEE J. Solid-State Circuits*, vol. 49, no. 12, pp. 3046–3062, Dec. 2014.
- [11] J. Zhou, T.-H. Chuang, T. Dinc, and H. Krishnaswamy, “Integrated wideband self-interference cancellation in the RF domain for FDD and full-duplex wireless,” *IEEE J. Solid-State Circuits*, vol. 50, no. 12, pp. 3015–3031, Dec. 2015.
- [12] T. Zhang, A. R. Suvarna, V. Bhagavatula, and J. C. Rudell, “An integrated CMOS passive self-interference mitigation technique for FDD radios,” *IEEE J. Solid-State Circuits*, vol. 50, no. 5, pp. 1176–1188, May 2015.
- [13] A. Goel, B. Analui, and H. Hashemi, “Tunable duplexer with passive feed-forward cancellation to improve the RX-TX isolation,” *IEEE Trans. Circuits Syst. I, Reg. Papers*, vol. 62, no. 2, pp. 536–544, Feb. 2015.
- [14] J. I. Choi, M. Jain, K. Srinivasan, P. Lewis, and S. Katti, “Achieving single channel, full duplex wireless communication,” in *Proc. 16th Annu. Int. Conf. Mobile Comput. Netw. (MobiCom)*, New York, NY, USA, 2010, pp. 1–12.
- [15] M. Mikhemar, H. Darabi, and A. A. Abidi, “A multiband RF antenna duplexer on CMOS: Design and performance,” *IEEE J. Solid-State Circuits*, vol. 48, no. 9, pp. 2067–2077, Sep. 2013.
- [16] B. van Liempd, B. Herschberg, B. Debaillie, P. Wambacq, and J. Craninckx, “An electrical-balance duplexer for in-band full-duplex with <-85dBm in-band distortion at +10dBm TX-power,” in *Proc. 41st Eur. Solid-State Circuits Conf. (ESSCIRC)*, Sep. 2015, pp. 176–179.
- [17] S. H. Abdelhaleem, P. S. Gudem, and L. E. Larson, “Tunable CMOS integrated duplexer with antenna impedance tracking and high isolation in the transmit and receive bands,” *IEEE Trans. Microw. Theory Techn.*, vol. 62, no. 9, pp. 2092–2104, Sep. 2014.
- [18] M. Elkholmy, M. Mikhemar, H. Darabi, and K. Entesari, “Low-loss integrated passive CMOS electrical balance duplexers with single-ended LNA,” *IEEE Trans. Microw. Theory Techn.*, vol. 64, no. 5, pp. 1544–1559, May 2016.
- [19] SKYFR-000709: 2110-2170 MHz Single Junction Robust Lead Circulator, Skyworks Solutions, Woburn, MA, USA, May 2013.
- [20] S. Tanaka, N. Shimomura, and K. Ohtake, “Active circulators—The realization of circulators using transistors,” *Proc. IEEE*, vol. 53, no. 3, pp. 260–267, Mar. 1965.
- [21] S. Wang, C. H. Lee, and Y. B. Wu, “Fully integrated 10-GHz active circulator and quasi-circulator using bridged-T networks in standard CMOS,” *IEEE Trans. Very Large Scale Integr. (VLSI) Syst.*, vol. 24, no. 10, pp. 3184–3192, Oct. 2016.
- [22] S. A. Ayati, D. Mandal, B. Bakaloglu, and S. Kiaei, “Adaptive integrated CMOS circulator,” in *Proc. IEEE Radio Freq. Integr. Circuits Symp. (RFIC)*, May 2016, pp. 146–149.
- [23] N. Reiskarimian and H. Krishnaswamy, “Magnetic-free non-reciprocity based on staggered commutation,” *Nature Commun.*, vol. 7, no. 4, Apr. 2016, Art. no. 11217.
- [24] G. Carchon and B. Nauwelaers, “Power and noise limitations of active circulators,” *IEEE Trans. Microw. Theory Techn.*, vol. 48, no. 2, pp. 316–319, Feb. 2000.
- [25] N. A. Estep, D. L. Sounas, J. Soric, and A. Alù, “Magnetic-free non-reciprocity and isolation based on parametrically modulated coupled-resonator loops,” *Nature Phys.*, vol. 10, no. 12, pp. 923–927, Dec. 2014.
- [26] N. A. Estep, D. L. Sounas, and A. Alù, “Magnetless microwave circulators based on spatiotemporally modulated rings of coupled resonators,” *IEEE Trans. Microw. Theory Techn.*, vol. 64, no. 2, pp. 502–518, Feb. 2016.
- [27] S. Qin, Q. Xu, and Y. E. Wang, “Nonreciprocal components with distributedly modulated capacitors,” *IEEE Trans. Microw. Theory Techn.*, vol. 62, no. 10, pp. 2260–2272, Oct. 2014.

- [28] A. Ghaffari, E. A. M. Klumperink, M. C. M. Soer, and B. Nauta, "Tunable high-Q N-path band-pass filters: Modeling and verification," *IEEE J. Solid-State Circuits*, vol. 46, no. 5, pp. 998–1010, May 2011.
- [29] C. Andrews and A. C. Molnar, "A passive mixer-first receiver with digitally controlled and widely tunable RF interface," *IEEE J. Solid-State Circuits*, vol. 45, no. 12, pp. 2696–2708, Dec. 2010.
- [30] D. Yang, C. Andrews, and A. Molnar, "Optimized design of N-phase passive mixer-first receivers in wideband operation," *IEEE Trans. Circuits Syst. I, Reg. Papers*, vol. 62, no. 11, pp. 2759–2770, Nov. 2015.
- [31] D. M. Pozar, *Microwave Engineering*. Reading, MA, USA: Addison-Wesley, 1990.
- [32] N. Reiskarimian, J. Zhou, T. H. Chuang, and H. Krishnaswamy, "Analysis and design of two-port N -path bandpass filters with embedded phase shifting," *IEEE Trans. Circuits Syst. II, Express Briefs*, vol. 63, no. 8, pp. 728–732, Aug. 2016.
- [33] H. Yuksel, D. Yang, and A. C. Molnar, "A circuit-level model for accurately modeling 3rd order nonlinearity in CMOS passive mixers," in *Proc. Radio Freq. Integr. Circuits Symp.*, Jun. 2014, pp. 127–130.



Negar Reiskarimian (S'15) received the B.Sc. and M.Sc. degrees in telecommunication systems and microelectronic circuits from the Sharif University of Technology, Tehran, Iran, in 2011 and 2013, respectively. She is currently pursuing the Ph.D. degree in electrical engineering with Columbia University, New York, NY, USA.

During her Master's studies, she was involved in design and implementation of a diversity receiver with maximum sensitivity for the electrical-optical interface of a free-space optics system. Her current research interests include the theory, design, and experimental validation of analog/RF/millimeter-wave integrated circuits and systems, with an emphasis on novel non-reciprocal components for emerging wireless communication paradigms.

Ms. Reiskarimian is a recipient of the 2016–2017 Qualcomm Innovation Fellowship, the 2016–2017 IEEE Solid-State Circuits Society (SSCS) Predoctoral Achievement Award, 2017 ISSCC Analog Devices (ADI) Outstanding Student Designer Award and 2017 IEEE Microwave Theory and Techniques Society (MTT-S) Graduate Fellowship.



Jin Zhou (S'11–M'17) received the B.S. degree in electronics science and technology from Wuhan University, Wuhan, China, in 2008, the M.S. degree in microelectronics from Fudan University, Shanghai, China, in 2011, and the Ph.D. degree in electrical engineering from Columbia University, New York, NY, USA, in 2017.

In 2017, he joined the Department of Electrical and Computer Engineering, University of Illinois at Urbana–Champaign, Champaign, IL, USA, as an Assistant Professor. His current research interests include integrated circuits and systems for wireless applications.

Dr. Zhou was a recipient of the 2010 IEEE International Conference on Solid-State and Integrated Circuit Technology Excellent Student Paper Award, the 2015–2016 Qualcomm Innovation Fellowship, and the 2015–2016 IEEE Solid-State Circuits Society Predoctoral Achievement Award. He received the 2015–2016 Jury Award from the Department of Electrical Engineering at Columbia University for outstanding achievement in the areas of systems, communications, signal processing, or circuits.



Harish Krishnaswamy (S'03–M'09) received the B.Tech. degree in electrical engineering from IIT Madras, Chennai, India, in 2001, and the M.S. and Ph.D. degrees in electrical engineering from the University of Southern California (USC), Los Angeles, CA, USA, in 2003 and 2009, respectively.

In 2009, he joined the Electrical Engineering Department, Columbia University, New York, NY, USA, where he is currently an Associate Professor. His current research interests include integrated devices, circuits, and systems for a variety of RF, mm-wave and sub-mm-wave applications.

Dr. Krishnaswamy serves as a member of the Technical Program Committee of several conferences, including the IEEE International Solid-State Circuits Conference (ISSCC) (2015/16–present) and the IEEE RFIC Symposium (2013–present). He is currently serving as an IEEE SSCS Distinguished Lecture for 2017 and 2018. He was a recipient of the IEEE ISSCC Lewis Winner Award for Outstanding Paper in 2007, the Best Thesis in Experimental Research Award from the USC Viterbi School of Engineering in 2009, the Defense Advanced Research Projects Agency Young Faculty Award in 2011, the 2014 IBM Faculty Award, and the 2015 IEEE RFIC Symposium Best Student Paper Award–1st Place.